Retrieval of Solar-induced Chlorophyll Fluorescence from Satellite Measurements: Comparison of SIF between TanSat and OCO-2

Lu Yao[1], Yi Liu[1], Dongxu Yang[1], Zhaonan Cai[1], Jing Wang[1], Chao Lin[2], Naimeng Lu[3], Daren Lyu[1], Longfei Tian[4], Maohua Wang[5], Zengshan Yin[4], Yuquan Zheng[2], Sisi Wang[6]

[1]Carbon Neutral Research Center & Key Laboratory of Middle Atmosphere and Global Environment Observation, Institute of Atmospheric Physics, Chinese Academy of Sciences, No. 40, Huayan Li, Chaoyang District, Beijing 100029, China
[2]Changchun Institute of Optics, Fine Mechanics and Physics, Changchun 130033, China
[3]National Satellite Meteorological Center, China Meteorological Administration, Beijing 100081, China
[4]Shanghai Engineering Center for Microsatellites, Shanghai 201203, China
[5]Shanghai Advanced Research Institute, Chinese Academy of Sciences, Shanghai 201210, China
[6]National Remote Sensing Center of China, Beijing 100036, China

Correspondence to: Dongxu Yang (yangdx@mail.iap.ac.cn)

Abstract. Solar-induced chlorophyll fluorescence (SIF) is emitted during photosynthesis in plant leaves. It constitutes a small additional offset to reflected radiance and can be observed by sensitive instruments with high signal-to-noise ratio and spectral resolution. The Chinese global carbon dioxide monitoring satellite (TanSat) acquires measurements of greenhouse gas column densities. The advanced technical characteristics of the grating spectrometer (ACGS) onboard TanSat enable SIF retrievals from observations in the O_2-A band. In this study, one year of SIF data was retrieved from Orbiting Carbon Observatory-2 (OCO-2) and TanSat measurements using the IAPCAS/SIF algorithm. A comparison between the IAPCAS/SIF results retrieved from OCO-2 spectra and the official OCO-2 SIF product (OCO2_Level 2_Lite_SIF.8r) shows a strong linear relationship ($R^2 > 0.85$) and suggests good reliability of the IAPCAS/SIF retrieval algorithm. Comparing global distributions of SIF retrieved by IAPCAS/SIF from TanSat and OCO-2 shows the same spatial pattern for all seasons with gridded SIF difference less than 0.3 W m^{-2} μm^{-1} sr^{-1}. The global distributions also agree well with the official OCO-2 SIF product with difference less than 0.2 W m^{-2} μm^{-1} sr^{-1}. The retrieval uncertainty of seasonally gridded TanSat IAPCAS/SIF is less than 0.03 W m^{-2} μm^{-1} sr^{-1} whereas the uncertainty of each sounding ranges from 0.1 to 0.6 W m^{-2} μm^{-1} sr^{-1}. The relationship between annually-averaged SIF products and FLUXCOM gross primary productivity (GPP) was also estimated for six vegetation types in a 1° × 1° grid over the globe, indicating that the SIF data from the two satellites have the same potential in quantitatively characterizing ecosystem productivity. The spatiotemporal consistency between TanSat and OCO-2 and their comparable data quality enable joint usage of the two mission products. Data supplemented by TanSat observations are expected to contribute to the development of global SIF maps with more spatiotemporal detail, which will advance global research on vegetation photosynthesis.

1 Introduction

Terrestrial vegetation ecosystems play a large role in the global carbon cycle through the processes of photosynthesis and respiration. Incoming radiation is absorbed, reflected, and/or transmitted by plant leaves. A portion of the absorbed radiation is used by the chlorophyll in plant leaves for carbon fixation, while the rest is either dissipated as heat or re-emitted as solar-induced chlorophyll fluorescence (SIF) at longer wavelengths (Frankenberg et al., 2011a, 2014). In contrast to the traditional remotely sensed vegetation indices obtained from some studies (Frankenberg et al., 2011b; Guanter et al., 2014; Li et al., 2018; Sun et al., 2017a; Yang et al., 2015; Zhang et al., 2014), SIF offers the potential to measure photosynthetic activity and gross primary production (GPP), due to the strong correlation between these measures (Frankenberg et al., 2011b; Guanter et al., 2012, 2014). The fluorescence emission adds a low-intensity radiance of less than 10 W m^{-2} μm^{-1} sr^{-1} and fills in the solar absorption features of the reflected spectrum (Frankenberg et al., 2011a). The filling-in effect of the solar lines (Fraunhofer lines) is the basic principle applied to measure SIF from space using the capabilities of hyperspectral observation (Frankenberg et al., 2011b; Guanter et al., 2012).

The first attempt of observing SIF from space was performed using images acquired by the Medium Resolution Imaging Spectrometer (MERIS) onboard the ENVIronmental SATellite (ENVISAT) (Guanter et al., 2007). This led to a new idea for conducting SIF studies on a global scale. The first global SIF map was retrieved from high-resolution spectra of the Greenhouse-gases Observing SATellite (GOSAT) (Joiner et al., 2011; Frankenberg et al., 2011b). After that, SIF retrievals were implemented for a variety of satellite measurements, such as those from the Global Ozone Monitoring Experiment-2 (GOME-2) instruments onboard meteorological operational satellites, SCIAMACHY onboard ENVISAT, and Orbiting Carbon Observatory-2 (OCO-2) (Joiner et al., 2016; Köhler et al., 2015). The TROPOspheric Monitoring Instrument (TROPOMI) onboard Sentinel 5 Precursor (S-5P) provides more efficient SIF observations in terms of global coverage and new opportunities for exploring the application potential of SIF data in the terrestrial biosphere as well as in climate research (Doughty et al., 2019; Köhler et al., 2018b). Furthermore, an upcoming European Space Agency mission called FLuorescence EXplorer (FLEX), the first satellite dedicated to SIF observation, will launch in the middle of 2024 (Drusch et al., 2017). Many studies on SIF applications have been initiated with the accumulation of SIF products in recent years. The responses of satellite-measured SIF to environmental conditions have been applied to drought dynamics monitoring and regional vegetation water stress estimation (Lee et al., 2013; Sun et al., 2015; Yoshida et al., 2015). As a proxy of photosynthesis, SIF acts as a powerful constraint parameter in estimating carbon exchange in an ecosystem between the atmosphere, ocean, and soil; as such, the analysis of the relationship between SIF and GPP has become an important research topic (Li et al., 2018; Köhler et al., 2018a; Sun et al., 2017a; Zhang et al., 2018). The strong linear relationship between them paves the way for improving terrestrial ecosystem model simulations of GPP, along with consequent improvement of global carbon flux estimation (MacBean et al., 2018; Yin et al., 2020). GPP estimations based on satellite-measured SIF have proven to be an effective method validated by in-situ flux observations (Joiner et al., 2018; Qiu et al., 2020). However, uncertainty in the factors that determine the relationship between SIF and GPP still exists and is a key limitation in the application of SIF to flux estimation. Based on

68 multi-satellite SIF products, eddy covariance flux tower observations, and ecological models, the relationship between SIF and
69 GPP under different environmental conditions has been discussed in a number of studies to analyze the dominant factors for
70 the growing status of different biomes, such as temperature, soil moisture, and vegetation types (Chen et al., 2020; Doughty et
71 al., 2019; Li et al., 2020; Qiu et al., 2020; Yin et al., 2020).

72 The Chinese global carbon dioxide monitoring satellite (TanSat) was launched in December 2016. Aiming at acquiring CO_2
73 concentrations similar to OCO-2, TanSat flies in a sun-synchronous orbit at approximately 700 km height with a 16-day repeat
74 cycle and an equator crossing time of ~1:30 p.m. local time (Cai et al., 2014; Liu et al., 2018; Yang et al., 2018). Onboard
75 TanSat, the hyperspectral Atmospheric Carbon-dioxide Grating Spectrometer (ACGS) is designed to separately record solar
76 backscatter spectra in three channels centered at 0.76 μm (O_2-A band), 1.61 μm (weak CO_2 absorption band), and 2.06 μm
77 (strong CO_2 absorption band). Many Optimal Estimation Method (OEM) full physics retrieval algorithms have been developed
78 and applied for the total column-averaged dry air CO2 mole fraction (XCO_2) retrievals (Bösch et al., 2006; O'Dell et al., 2012;
79 Reuter et al., 2010; Yang et al., 2015b; Yoshida et al., 2011, 2013). The Institute of Atmospheric Physics Carbon Dioxide
80 Retrieval Algorithm for Satellite Remote Sensing (IAPCAS) algorithm has been applied for TanSat XCO2 retrievals (Yang et
81 al., 2018; Yang et al., 2021) and was also previously tested on spectra from the GOSAT and OCO-2 missions (Yang et al.,
82 2015b). However, the fluorescence feature causes substantial biases when retrieving surface pressure and scattering parameters
83 from the O_2-A band, and the associated errors propagate into the XCO_2 retrievals. In previous XCO_2 retrievals, the surface
84 emissions were well modeled as a continuum offset of the O_2-A band to reduce errors (Frankenberg et al., 2011a, 2012; Joiner
85 et al., 2012). For TanSat, its high spectral resolution of ~0.044 nm and a signal-to-noise ratio of ~360 in the O_2-A band makes
86 it possible to obtain SIF, with a spatial resolution of 2 km × 2 km in nadir mode (Liu et al., 2018).

87 Various approaches have been used to infer SIF from satellite measurements (Frankenberg et al., 2011b, 2014a, 2014b; Guanter
88 et al., 2007, 2012, 2015; Joiner et al., 2011, 2013, 2016; Köhler et al., 2015, 2018b). The SIF signal induces a filling-in effect
89 of solar lines, which can be used for SIF retrieval, as the fractional depth of solar Fraunhofer lines does not change during
90 radiation transmission in the atmosphere. To be able to measure the filling-in features from SIF, high-resolution spectra are
91 required to describe subtle changes in the spectral absorption lines. Given highly resolved spectral features, a method was
92 developed based on solar line fitting and the Beer-Lambertian law. This method is robust and accurate when the spectrum is
93 out of the influence of telluric absorptions, even in the presence of aerosols (Frankenberg et al., 2011a; Joiner et al., 2011); in
94 the current study, this method was applied to develop the IAPCAS/SIF algorithm. Another SIF retrieval method is the data-
95 driven algorithm based on the singular value decomposition (SVD) technique (Joiner et al., 2011; Guanter et al., 2012), which
96 has been broadly applied to GOSAT, OCO-2, TanSat and TROPOMI (Joiner et al., 2011; Guanter et al., 2012, 2015;
97 Frankenberg et al., 2014a; Du et al., 2018; Köhler et al., 2018b). In the data-driven method, the spectrum is represented as a
98 linear combination of the SIF signal and several singular vectors that are trained from non-fluorescent scenes by SVD; thus,
99 the SIF signal can be obtained with linear least-squares fitting (Du et al., 2018; Guanter et al., 2012). The first TanSat SIF
100 map was obtained by the SVD method (Du et al., 2018). In a previous study, a new TanSat SIF product retrieved by
101 IAPCAS/SIF algorithm was introduced and the two kinds of TanSat SIF products by IAPCAS/SIF and the SVD methods were

102 compared (Yao et al., 2021). The preliminary comparison between the two TanSat SIF products showed that the two SIF

103 products share a similar global pattern and signal magnitude for all seasons while different biases still exist in four seasons

104 (Yao et al., 2021). The different biases in the four seasons may be caused by the different training samples of the SVD method,

105 which indicates that the training samples have a significant impact on the retrieval results. In order to obtain stable SIF data

106 products from TanSat and other subsequent satellite missions, it is particularly important to establish a stable and high-

107 precision SIF inversion algorithm. To further validate the IAPCAS/SIF algorithm and to test the potential for synergistic,

108 multi-satellite SIF analysis, in this study, we detail the IAPCAS/SIF algorithm for TanSat and we compare the SIF products

109 from TanSat and OCO-2 for a range of spatiotemporal scales.

110 2 Data and retrieval algorithm

111 2.1 Retrieval Principle and Method

112 We used TanSat version 2 Level 1B (L1B) nadir-mode earth observation data in the retrieval process. The measurements

113 covered the period from March 2017 to February 2018. Polarized radiance in the O_2-A band with a spectral resolution of 0.044

114 nm was provided in the L1B data, and two micro-windows near 757 nm (758.3-759.2 nm) and 771 nm (769.6-770.3 nm) were

115 chosen to retrieve top-of-atmosphere (TOA) SIF while avoiding the contamination from strong lines of atmospheric gas

116 absorption. The retrieval was independent for each micro-window as shown in Figure 1. To avoid duplication of information,

117 we use the SIF product at 757 nm as the example in the analysis.
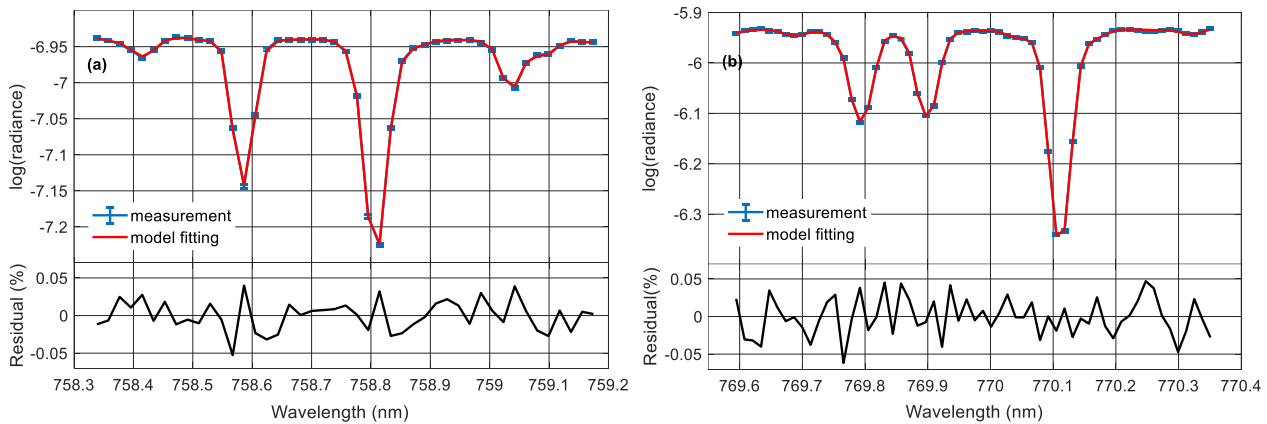
119 **Figure 1: The fitted spectra and residuals for the (a) 757 nm and (b) 771 nm micro-windows of TanSat measurement. The error bar**
120 **of the measured spectra depicts the estimated precision of each TanSat sounding.**

122 Filling-in on solar lines by chlorophyll fluorescence in the O_2-A band can be detected in the hyperspectral measurements from

123 TanSat. This effect on spectral radiance is different from the impact of atmospheric and surface processes, e.g., scattering and

124 absorption. For example, scattering by aerosols and clouds does not change the relative depth of clear solar lines, unlike the

125   SIF emission signal. We applied the differential optical absorption spectroscopy (DOAS) technique to IAPCAS/SIF algorithm

126   for TanSat measurement (Frankenberg, 2014b; Sun et al., 2018).

127   The TOA spectral radiance (L_{TOA}^λ) at wavelength λ can be represented as follows:

128    $$L_{TOA}^\lambda = I_t^\lambda \cdot \mu_0 \cdot \left(\rho_0^\lambda + \frac{\rho_s^\lambda \cdot T_\downarrow^\lambda \cdot T_\uparrow^\lambda}{\pi}\right) + F_{TOA}^\lambda \tag{1}$$

129   where I_t^λ is the incident solar irradiance at the TOA, μ_0 is the cosine of the solar zenith angle (SZA), ρ_0^λ is atmospheric path

130   reflectance, ρ_s^λ is surface reflectance, and $T_\downarrow^\lambda$ and $T_\uparrow^\lambda$ are the total atmospheric transmittances along the light-path in the

131   downstream and upstream directions, respectively. F_{TOA}^λ is the SIF radiance at TOA.

132   The first term on the right of Eq. (1) represents the transmission process of solar radiance. In the micro-windows used in SIF

133   retrieval, gas absorption is very weak and smooth, and hence, the atmosphere term $\mu_0 \cdot \left(\rho_0^\lambda + \frac{\rho_s^\lambda \cdot T_\downarrow^\lambda \cdot T_\uparrow^\lambda}{\pi}\right)$ can be simplified to a

134   low-order polynomial $\sum_{i=0}^n a_i \cdot \lambda^i$ that varies with λ (Joiner et al., 2013; Sun et al., 2018); this is always valid as long as the

135   spectrum fitting range is out of sharp atmospheric absorptions. Then Eq. (1) could be represented as:

136    $$L_{TOA}^\lambda(F_{TOA}^\lambda, \boldsymbol{a}) = <I_t^\lambda> \cdot \sum_{i=0}^n a_i \cdot \lambda^i + F_{TOA}^\lambda \tag{2}$$

137   where $<>$ denote the convolution with the ISRF from line-by-line spectra, and the coefficient vector $\boldsymbol{a}$ determines the

138   wavelength dependence polynomial for the atmosphere term.

139   To facilitate the extraction of SIF signals, the radiance is normalized to the continuum level radiance and the relative

140   contribution of SIF to the continuum level radiance F_s^{rel} is defined. In the micro-window, SIF was regarded as a constant signal

141   due to its small changes. When the spectral radiance measurement was converted to logarithmic space, the forward model was

142   expressed as:

143    $$f(F_s^{rel}, \boldsymbol{b}) = log(<I_t + F_s^{rel}>) + \sum_{i=0}^n b_i \cdot \lambda^i \tag{3}$$

144   Where I_t is a normalized disk-integrated solar transmission model. The vector $\boldsymbol{b}$ consists of the polynomial coefficients b_i

145   and we used a second-order polynomial ($i = 0, 1, 2$) in the retrieval.

146   Although the atmospheric gas absorption was very weak in the micro-window, the weak absorption and the far-wing effects

147   (O_2 lines) can still change spectral features, which induces errors in spectrum fitting. In other physics-based retrievals, the

148   surface pressure data of the European Centre for Medium-Range Weather Forecasts (ECMWF) together with topographic data

149   are usually used as the true surface pressure to simulate the atmospheric transmission in the range of the O_2-A band. However,

150   there is still a difference between the true surface pressure and the model surface pressure, so we introduced a factor here to

151   reduce the influence of the inaccurate surface pressure. In the IAPCAS/SIF algorithm, we use the ECMWF interim surface

152   pressure ($0.75° \times 0.75°$) to estimate O_2 absorption first and then modify the absorption feature by a scale factor. The scale

153   factor is obtained simultaneously in SIF retrieval to reduce the error induced by the uncertainty in surface pressure. As

154   described by Yang (2020), there is also a continuum feature in TanSat L1B data that needs to be considered for the high-quality

155   fitting of the O_2-A band. However, in this study, this continuum feature was not corrected, as the impact of such a smooth

156 continuum variation in the micro-window is weak and the polynomial continuum model is capable of compensating for most

157 of this effect.

158 The state vector includes the relative SIF signal F_s^{rel}, a wavenumber shift, the scale factor for the O_2 column absorption, and

159 coefficients of the polynomial. The continuum level radiance I_{cont} within the fitting window is calculated using the radiance

160 outside the absorption features in the micro-window and is then used for the actual SIF signal calculation thus: $F = F_s^{rel} \cdot I_{cont}$.

161 In the IAPCAS/SIF algorithm, we used an OEM for state vector optimization in the retrieval process. Compared to the IAPCAS

162 XCO$_2$ retrieval, the IAPCAS/SIF retrieval employs a state vector with fewer elements and a much simpler forward model, so

163 there is no need to perform complex radiative transfer calculations. Considering the low complexity of SIF retrieval, the Gauss-

164 Newton method was applied iteratively to find the optimal solution.

2.2 Bias Corrections

166 A systematic error remains in the raw SIF retrieval output if no bias correction is performed; similar results have been reported

167 in GOSAT and OCO-2 SIF retrieval studies (Frankenberg et al., 2011a, 2011b; Sun et al., 2018). This is because the SIF signal

168 is weak (e.g., typically ~1-2% of the continuum level radiance), which means that even a small issue in the measurement, such

169 as a zero-offset caused by radiometric calibration error, could induce significant bias. Unfortunately, the lack of knowledge on

170 in-flight instrument performance makes it difficult to perform a direct systematic bias correction in the measured spectrum.

171 The bias was considered to be related to the continuum level radiance in the previous works. To get the relationship between

172 the continuum level radiance and the bias, we calculated the mean bias for continuum level radiance at the interval of 5 W m^{-2}

173 μm^{-1} sr^{-1} from all non-fluorescence measurements, and then a piecewise linear function fit was applied to describe the

174 relationship between the continuum level radiance and the biases.

175 The non-fluorescence soundings that were used in the bias estimation were based on the dataset "sounding_landCover" in

176 TanSat L1B data. This dataset depends on the MODIS land cover product and provides a scheme consisting of 17 land cover

177 classifications defined by the International Geosphere-Biosphere Programme. The measurements marked as "snow and ice,"

178 "barren," and "sparsely vegetated" were chosen to estimate the bias. Calibrations compensated for most of the instrument

179 degradations, but this alone was not perfect. To reduce the impact from the remaining minor discrepancies, we built the bias

180 correction function daily to obtain bias for each sounding via interpolation of the continuum level radiance (Sun et al., 2017b,

181 2018).

182 The bias curves shown in Figure 2 differ significantly between TanSat and OCO-2. This is mostly due to the differences in

183 instrument performance and radiometric calibration. In general, the TanSat bias curves exhibited two peaks at radiance levels

184 of approximately 40 and 125 W m^{-2} μm^{-1} sr^{-1}, separately, and most biases were larger than 0.015. For OCO-2, the curves

185 dropped sharply at low radiance levels, reaching the valley at a radiance level of approximately 40 W m^{-2} μm^{-1} sr^{-1}, and then

186 increased slowly with the radiance level.
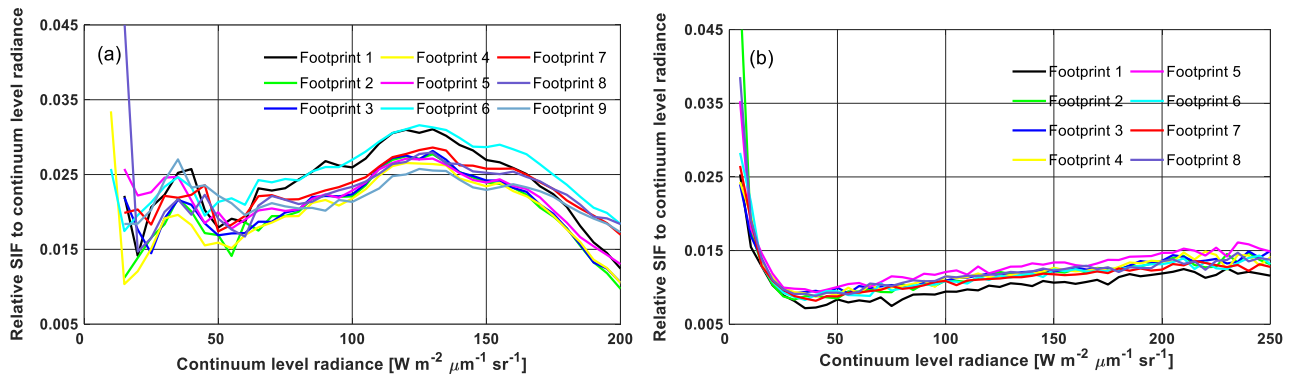
Figure 2: Variations in the bias correction curves of continuum level radiance from (a) TanSat on July 7, 2017, and (b) Orbiting Carbon Observatory-2 (OCO-2) on June 16, 2017. The different colors in the legend present different footprints of the satellite frame.

2.3 Data Quality Controls

Only data that passed quality control were used in further applications. There were two data quality control processes for the SIF products: pre-screening and post-screening. Pre-screening focused mainly on cloud screening; only cloud-free measurements were used in SIF retrieval. A surface pressure difference (SPD), defined as:

$$\Delta P_0 = |P_{retrieval} - P_{ECMWF}| \tag{3}$$

was used to evaluate cloud contamination along with a chi-square test

$$\chi^2 = \sum \frac{(y_{sim} - y_{obs})^2}{y_{noise}^2} \tag{4}$$

where y_{sim}, y_{obs}, and y_{noise} represent the model fitting spectrum, observation spectrum, and spectrum noise, respectively. $P_{retrieval}$ is the apparent surface pressure obtained from O_2-A band surface pressure retrieval, assuming a Rayleigh-scattering atmosphere. P_{ECMWF} is the surface pressure data from the ECMWF interim ($0.75° \times 0.75°$) reanalysis data product (Dee et al., 2011), which is interpolated to the sounding location and corrected for elevation differences with the Shuttle Radar Topography Mission Global 30 Arc-Second Elevation digital elevation model (DOI: 10.5067/MEaSUREs/SRTM/SRTMGL30.002). A "cloud-free" measurement was required to simultaneously satisfy an SPD of less than 20 hPa and a χ^2 value of less than 80. Here, post-screening was applied to filter out "bad" retrievals; this screening process involved the following steps: (1) SIF retrievals with reduced χ^2 (χ_{red}^2) values ranging from 0.7 to 1.3 were considered "good" fitting, (2) continuum level radiance outside the range of $15 \sim 200$ W m^{-2} μm^{-1} sr^{-1} was screened out to avoid scenes too bright or too dark, and (3) soundings with the SZA higher than 60° were also filtered out.

2.4 IAPCAS versus IMAP-DOAS OCO-2 SIF Retrieval

Before applied to TanSat retrievals, we tested the IAPCAS/SIF algorithm on the OCO-2 L1B data first (OCO2_L1B_Science.8r) and then compared the retrieval results with the OCO-2 L2 Lite SIF product (OCO2_Level

211 2_Lite_SIF.8r) retrieved by the Iterative Maximum A Posteriori-Differential Optical Absorption Spectroscopy (IMAP-DOAS)

212 algorithm (Frankenberg, 2014b). The Lite product provides the SIF value for each sounding and hence the SIF comparison

213 could be performed on the sounding scale for each month.

214 Table 1 displays the relationship of OCO-2 SIF values between the IAPCAS/SIF and IMAP-DOAS at 757 nm micro-window

215 for each month. Overall, the two SIF products were in good agreement. The linear fitting of the two SIF products suggests that

216 they are highly correlated, as indicated by the strong linear relationship with R^2 mostly larger than 0.85 and the root mean

217 square error (RMSE) of about 0.2 W m^{-2} μm^{-1} sr^{-1}. Good consistency between the two SIF products implies the reliability of

218 the IAPCAS/SIF algorithm; thus, it was further applied to TanSat SIF retrieval. However, there was still a small bias in the

219 comparisons, which was due, most likely, to the impact of differences in the bias correction method, retrieval algorithm, and

220 fitting window.

221 **Table 1:** Summary of the relationship between the IAPCAS OCO-2 and IMAP-DOAS OCO-2 solar-induced chlorophyll fluorescence

222 (SIF) products at 757nm micro-window.

month	Number of soundings	Slope	Intercept	R^2	RMSE/ W m^{-2} μm^{-1} sr^{-1}
2017/03	1097277	0.85	0.034	0.86	0.18
2017/04	1119464	0.86	0.045	0.87	0.19
2017/05	1054235	0.88	0.041	0.88	0.19
2017/06	1014848	0.91	0.032	0.90	0.19
2017/07	965309	0.92	0.011	0.91	0.19
2017/09	211219	0.88	0.005	0.81	0.23
2017/10	473359	0.88	0.031	0.88	0.17
2017/11	579009	0.87	0.022	0.85	0.19
2017/12	645134	0.87	0.020	0.88	0.16
2018/01	788655	0.87	0.019	0.88	0.17
2018/02*	629995	0.86	0.024	0.87	0.18

223 * Due to the lack of OCO-2 measurements in August 2017, the comparison is only performed for 11 months.

224 **3 Results and Discussion**

225 **3.1 Comparison between TanSat and OCO-2 SIF Measurements**

226 The comparison between TanSat and OCO-2 SIF measurements is a useful and powerful method for further verification of the

227 IAPCAS/SIF algorithm. The reason for adopting OCO-2 data is that OCO-2 and TanSat have similar observation modes,

228 including scanning method, transit time, spatial resolution, spectral resolution, and spectral range. The similarities mean that

229 the SIF product from the two satellite missions can be directly compared. Directly comparing OCO-2 and TanSat SIF

230 measurements could provide information on joint data application at the sounding scale for further studies. However, an

231 identical sounding overlap barely exists because the two satellites often have different nadir tracks on the ground, which is

232 induced by the different temporal and spatial intervals of the two satellite missions. Fortunately, the ground tracks of the two

satellites were relatively close from April 17 to April 23, 2017. A couple of overlapping orbits were found in the measurements obtained from Africa with the orbit number of 1733 from TanSat and 14890a from OCO-2 (Figure 3). In the comparison, the OCO2_Level 2_Lite_SIF.8r product was used to present the SIF emission over the study area. These overlapping measurements encompassed multiple land cover types, in which the SIF varied within an acceptable time difference (<5 min). Overall, measurements from the two satellites indicated SIF variation with land cover type. The SIF emission over evergreen broadleaf forests was larger than that over savannas, and grasslands exhibited the lowest SIF emission in April (Figure 3a,b). The mean SIF emission over evergreen broadleaf forests was approximately 0.9-1.1 W m^{-2} μm^{-1} sr^{-1}, whereas those over savannas and grasslands were 0.5-0.7 W m^{-2} μm^{-1} sr^{-1} and less than 0.1 W m^{-2} μm^{-1} sr^{-1}, respectively (Figure 3c,d). Furthermore, we also found a significant difference in the SIF emission intensity over tropical savannas, which was observed by both satellites (Figure 3c,d).
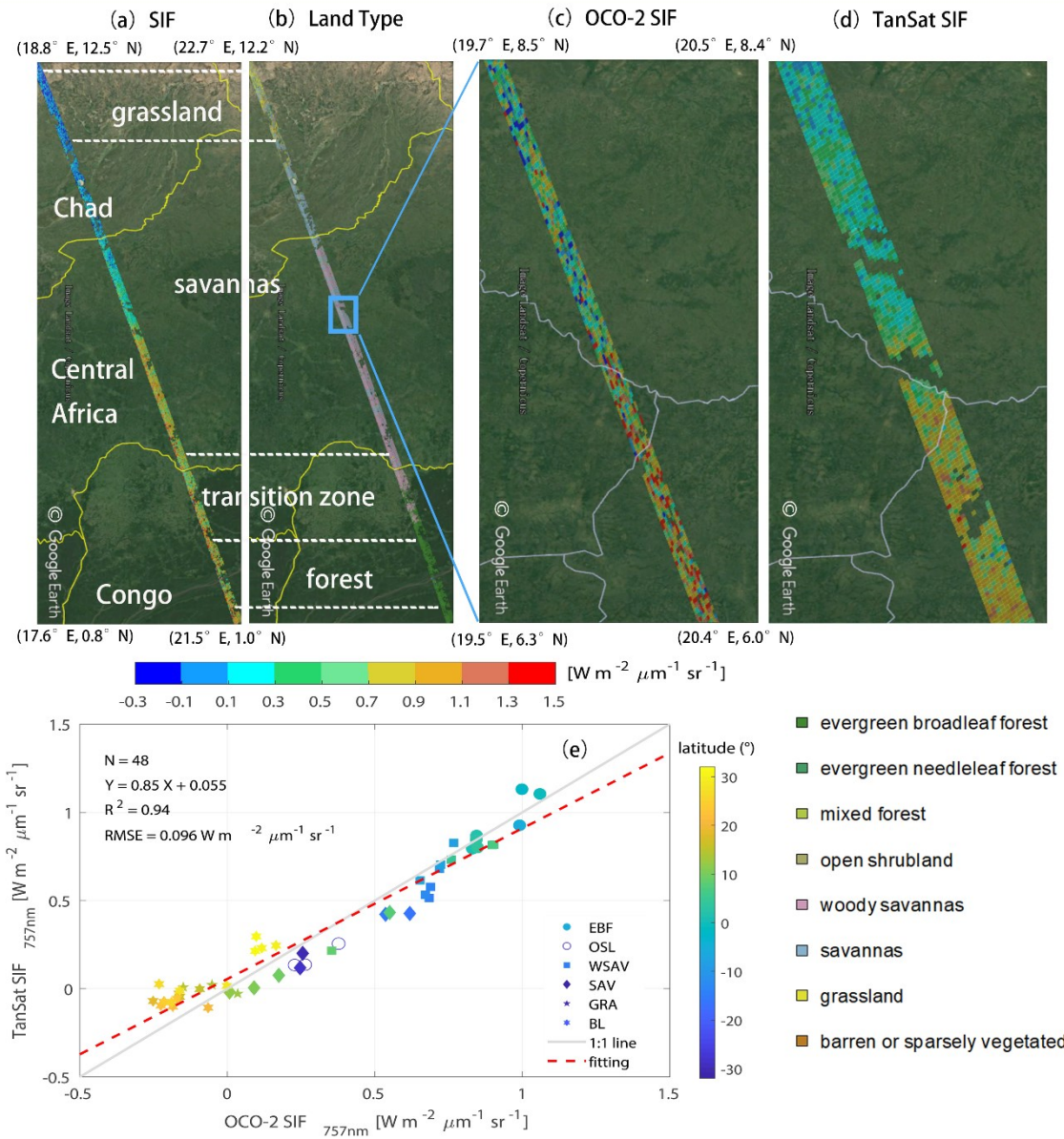
Figure 3: Overlapping orbits of TanSat and OCO-2 on April 19, 2017 over Africa displayed in Google Earth, (a) the SIF measurements from both satellites and (b) the footprint land cover type were compared. Compared to OCO-2, TanSat has a wider swath width. A zoom-in view over savannas shows variations in the SIF signal measured by (c) OCO-2 and (d) TanSat. The land surface image shown in Google earth is provided by Landsat/Copernicus team. Following the International Geosphere-Biosphere Programme classification scheme, the vertical legend on the bottom right corner depicts the land cover type that occurs in the study area. The middle horizontal color bar represents the intensity of the SIF radiance. (e) Small-area SIF comparison between OCO-2 and TanSat; each data point represents the mean SIF of a degree in latitude (colors) along the track. The marker legend that is shown on the bottom right of the plot indicates the dominant land cover (defined as the majority land cover type of each sounding) in each small area. There are six land cover types including evergreen broadleaf forest (EBF), open shrubland (OSL), woody savanna (WSAV), savanna (SAV), grassland (GRA), and barren land (BL). The red dashed line represents the linear fit between the two SIF products with statistics shown in the upper left of the plot. The gray line indicates a 1:1 relationship for reference.

10

257

258 Because the footprint sizes of the two satellites are different, it is difficult to make a direct footprint-to-footprint comparison.

259 Therefore, we made the comparison between the two satellite measurements based on a small area average. Each small area

260 spans a degree in latitude and continues along the track. The small area-averaged SIF comparison is shown in Figure 3e. The

261 results indicate good agreement, with an R^2 of 0.94 and an RMSE of 0.096 W m^{-2} μm^{-1} sr^{-1}. Additional ground-based SIF

262 measurement setups (Guanter et al., 2007; Liu et al., 2019; van der Tol et al., 2016; Yang et al., 2015a; Yu et al., 2019) should

263 allow for direct evaluation of satellite retrieval accuracy in the future.

264
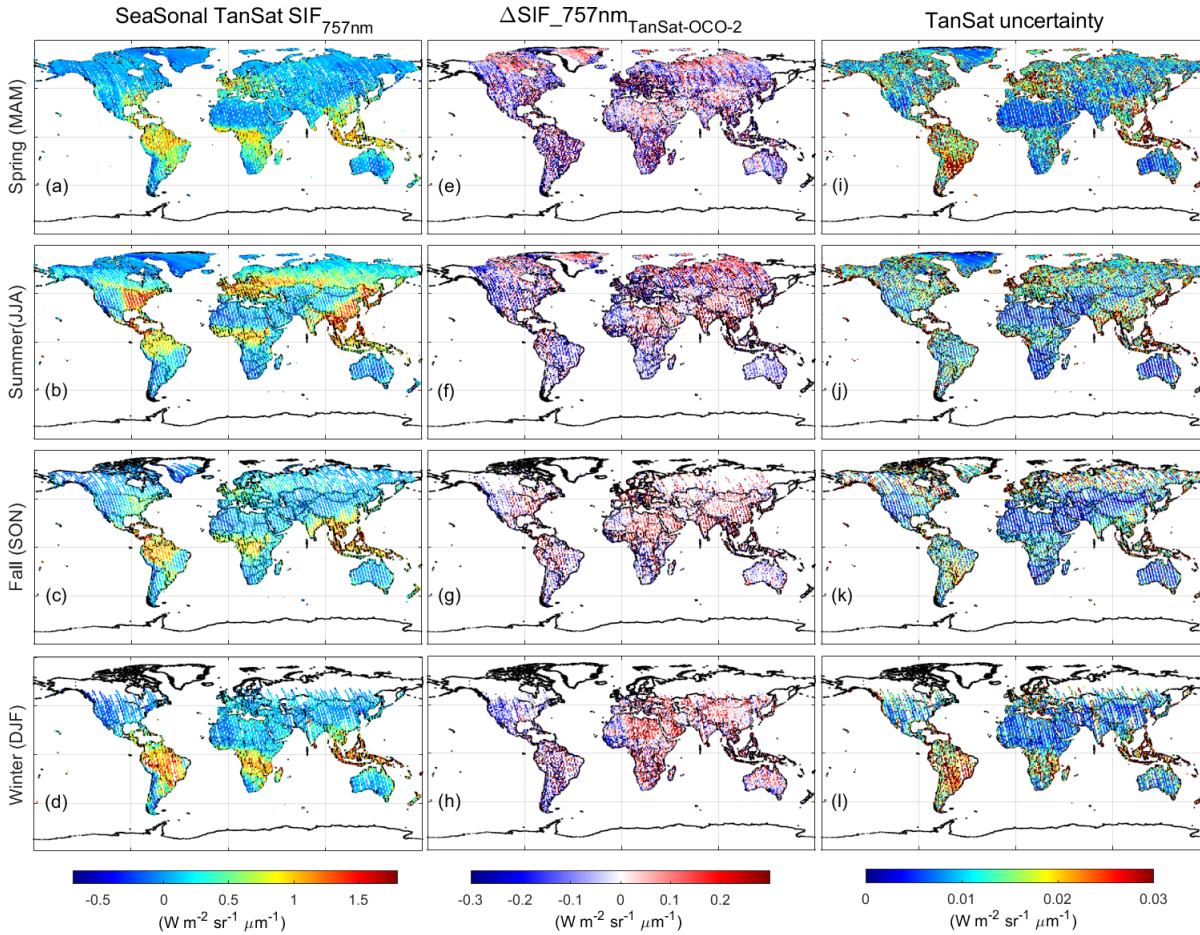
265

266 **Figure 4: Global TanSat SIF (left, a-d), differences between TanSat and IAPCAS OCO-2 SIF values (middle, e-h), and the grid-cell**
267 **retrieval uncertainty estimated from TanSat (right, i-l) at 1° × 1° spatial resolution. The maps in each row represent a Northern**
268 **Hemisphere season, i.e., spring (MAM), summer (JJA), fall (SON), and winter (DJF).**

269

11

270 Figure 4 shows the global SIF comparison between IAPCAS/SIF retrieved from OCO-2 and TanSat; this comparison is only

271 performed at $1° × 1°$ spatial resolution. In general, the difference in SIF globally is mostly less than 0.3 W m^{-2} μm^{-1} sr^{-1} for

272 all seasons, and on average, the smallest difference appears in fall. There are regional biases observed in North Africa, South

273 Africa, South America, and Europe in all seasons except fall. This is mainly caused by the differences in instrument

274 performance between TanSat and OCO-2, such as the Instrument Spectral Respond and the Signal-to-Noise. The instrument

275 performance difference is represented by the different structural characteristics of the bias curves. The bias correction

276 compensates for most of the bias caused by instrument performance; however, small biases could remain. Furthermore, the

277 hundreds of kilometers of distance between the OCO-2 and TanSat footprints, for example, over different vegetation regions,

278 will also cause some measurement discrepancies. The global distribution of the two satellites was also compared with the

279 official OCO-2 SIF data on the global scale, the results show that the difference between the retrieved SIF maps and the official

280 map is less than 0.2 W m^{-2} μm^{-1} sr^{-1}, indicating that the retrieved SIF data from OCO-2 and TanSat both have good SIF

281 characterization capabilities on a global scale. The uncertainty σ of each sounding was estimated to validate SIF reliability and

282 is provided in the product. σ is derived from the retrieval error covariance matrix, $S_e = (K^T S_0^{-1} K)^{-1}$, where K is the Jacobian

283 matrix from the forward model fitting and S_0 is the measurement error covariance matrix that is calculated from the instrument

284 spectrum noise. In general, σ ranges from 0.1 to 0.6 W m^{-2} μm^{-1} sr^{-1} for both TanSat and OCO-2 measurements in the 757

285 nm fitting window, which is of a similar magnitude and data range as those of previous studies (Du et al., 2018; Frankenberg

286 et al., 2014a). Meanwhile, the standard error of the mean SIF in each grid $σ_{meas}$ was estimated to represent the gridded retrieval

287 error and natural variability, which is calculated from TanSat SIF values with $σ_{meas} = \frac{σ_{std}}{\sqrt{n}}$ and $σ_{std} = \sqrt{\frac{\sum_{i=1}^{n}(SIF_i - \overline{SIF})^2}{n}}$, where

288 $σ_{std}$ represents the standard deviation of the grid cell with n soundings, SIF_i is the retrieved SIF values of each sounding,

289 and $\overline{SIF}$ is the mean SIF value for all measurements in the grid. As depicted in the right column of Figure 4, the $σ_{meas}$ of each

290 grid cell is much lower than the precision of a single sounding. The $σ_{meas}$ for South America is larger than that for any other

291 region on the globe (Figure 4i-l). This is similar to that of OCO-2 SIF retrieval and caused by fewer effective measurements

292 due to the South Atlantic Anomaly (Sun et al., 2018). The difference in SIF emission values between the two satellites indicates

293 that the synergistic use of two satellite SIF products still requires analysis of the impact of instrument differences, although

294 the two satellite SIF products share the same spatiotemporal pattern on a global scale.

3.2 SIF Global Distribution and Temporal Variation

296 The SIF emission intensity reflects the growth status of vegetation, and hence the overall global vegetation status can be

297 represented by global SIF maps for each season. TanSat SIF over a whole year's cycle, from March 2017 to February 2018, is

298 represented seasonally as a $1° × 1°$ grid spatially. The seasonal variation in SIF emission is clear in the Northern Hemisphere,

299 i.e., it is enhanced from spring to summer and then decreases (Sun et al., 2018).

300 In general, the SIF emission varied with latitude and the vegetation-covered areas near the equator maintained a continuous

301 SIF emission throughout the year. Large SIF emissions in the Northern Hemisphere, above 1.5 W m^{-2} μm^{-1} sr^{-1}, mostly from

302   the eastern U.S., southeast of China, and southern Asia in summer, were due to the large areas of cropland. There was also an

303   obvious SIF emission of 1-1.2 W m^{-2} μm^{-1} sr^{-1} observed over Central Europe and northeastern China during the summer. In

304   these regions, croplands and deciduous forests contribute to SIF emissions. In the Southern Hemisphere, the strongest SIF

305   emission occurred in the Amazon, with a level of approximately 1-2 W m^{-2} μm^{-1} sr^{-1} in DJF (Northern Hemisphere winter),

306   where there is an evergreen broadleaf rainforest. Africa, which is covered by evergreen broadleaf rainforests and woody

307   savannas, had an average SIF value of 0.7-1.5 W m^{-2} μm^{-1} sr^{-1} during the year.

308   The SIF-GPP relationship over different vegetation types was also investigated by comparing the annual mean satellite SIF

309   measurements with the FLUXCOM GPP (Jung et al., 2020; Tramontana et al., 2016) dataset in a 1° × 1° grid over the globe.

310   The FLUXCOM GPP dataset used in the study comprises monthly global gridded flux products with remote sensing and

311   meteorological/climate forcing (RS+METEO) setups, which are derived from mean seasonal cycles according to MODIS data

312   and daily meteorological information (Jung et al., 2020; Tramontana et al., 2016). In the correlation analysis, the high spatial

313   resolution (0.5°× 0.5°) of the FLUXCOM GPP was first resampled to 1°× 1° to keep the same temporal-spatial scale of SIF

314   and GPP data. The satellite-measured SIF is an instantaneous emission signal that varies with incident solar radiance within

315   the day. To reduce the differences caused by the observation time and SZA at different latitudes, we applied a daily adjustment

316   factor to convert the instantaneous SIF emission into a daily mean SIF (Du et al., 2018; Frankenberg et al., 2011b; Sun et al.,

317   2018). The daily adjustment factor d is calculated as follows:

318    $$d = \frac{\int_{t=t_0-12h}^{t=t_0+12h} \cos(SZA(t)) \cdot dt}{\cos(SZA(t_0))} \tag{5}$$

319   where t_0 is the observation time in fractional days and $SZA(t)$ is a function of latitude, longitude, and time for calculating the

320   SZA of the measurements. The annual averaged SIF is calculated from the daily mean SIF. To evaluate the relationship

321   between SIF and GPP on the periodic scale of vegetation growth status, annually-averaged data were used in the regression

322   fitting analysis.
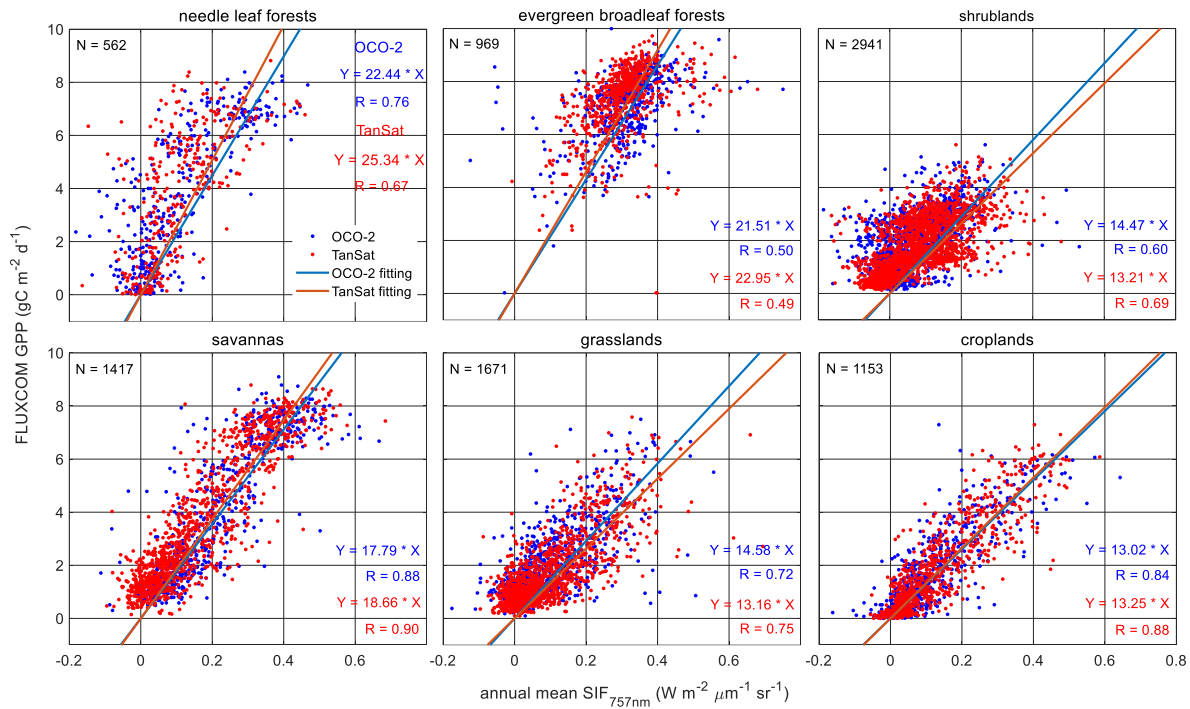
Figure 5: Relationship between annual mean SIF and FLUXCOM gross primary production (GPP) from March 2017 to February 2018. Blue and red dots represent OCO-2 and TanSat SIF grids, respectively. Fitted lines and statistics for OCO-2 and TanSat are shown in each plot.

Figure 5 shows the linear fits for six vegetation types, including needle leaf forest, evergreen broadleaf forest, shrubland, savanna, grassland, and cropland. Recent studies have shown a strong linear correlation between SIF and GPP. The TanSat SIF and the OCO-2 official SIF data were used to estimate the SIF-GPP correlation. To make a direct comparison of the relationship between SIF and GPP among various vegetation types, we used non-offset linear fitting to indicate the correlation between satellite SIF and FLUXCOM GPP. For savanna and cropland, there were strong relationships between the mean SIF and GPP with an R-value above 0.84. The fitting results show that the SIF products of the two satellites have similar capabilities in characterizing GPP, especially for the evergreen broadleaf forest, savanna, and cropland, with slopes of approximately 21, 18, and 13, respectively. For shrubland and grassland, the slope of OCO-2 SIF with GPP is higher than that of TanSat and has a worse correlation. For forests, OCO-2 SIF presents a better correlation with GPP, especially in the needle leaf forest. As a whole, for the same vegetation type, the SIF-GPP correlations for the two satellites are rather similar, indicating that the two satellite SIF products have similar capabilities in characterizing GPP. It shows the strong feasibility of the comprehensive application of different satellite SIF products. For different vegetation types, the SIF-GPP correlations were significantly different, indicating the different ability of SIF to characterize GPP of different vegetation. It represents that vegetation type is a key factor in determining the SIF-GPP relationship. The markedly different fitting slopes across various biomes suggest that the application of SIF in GPP estimation needs more detailed analysis although the evidence of the strong linear relationship between them.

14

4 Conclusions

In this paper, we introduced the retrieval algorithm IAPCAS/SIF and its application in TanSat and OCO-2 measurements. One year (March 2017-February 2018) of TanSat SIF data was introduced and compared with OCO-2 measurements in this study. The TanSat and OCO-2 SIF products based on the IAPCAS/SIF algorithm are available on the Cooperation on the Analysis of carbon SAtellites data (CASA) website, www.chinageoss.org/tansat. Comparing TanSat and OCO-2 measurements directly, using a case study, and indirectly, with global 1°×1° grid data, showed consistency between the two satellite missions, indicating that the coordinated usage of the two data products is possible in future studies. The correlation analysis between SIF and GPP further verified the feasibility of the synergistic application of SIF products from different satellite missions. Meanwhile, it should be noticed that the difference in the ability of satellite SIF products to characterize different vegetation types in data applications. With more satellites becoming available for SIF observations, space-based SIF observations have recently expanded in range to provide broad spatiotemporal coverage. The next-generation Chinese carbon monitoring satellite (TanSat-2) is now in the preliminary design phase, which is designed to be a constellation of six satellites to measure different kinds of greenhouse gases and trace gases in a more efficient way, including CO_2，CH_4, CO, NOx, as well as SIF. SIF measurements from TanSat-2 will provide global data products over broader coverage areas with less noise. The improvement in the spatiotemporal resolution of SIF data will benefit GPP predictions based on the numerous studies of the linear relationship between SIF and GPP. In future work, the measurement accuracy should be validated directly using ground-based measurements to ensure data quality.

Data availability

The SIF products of TanSat and OCO-2 by IAPCAS/SIF algorithm are available on the Cooperation on the Analysis of carbon SAtellites data (CASA) website (http://www.chinageoss.cn/tansat/index.html).

Author contributions

L.Y. and D.Y. developed the retrieval algorithm, designed the study, and wrote the paper. Y.L. led the SIF data process and analysis. Y.L., D.Y., Z.C., and J.W. contributed to manuscript organization and revision. C.L. and Y.Z. provided information on the TanSat instrument performance. L.T. provided TanSat in-flight information. M.W. and S.W. provided information on the scientific requirement for data further application. N.L. and D.L. led the TanSat data application. Z.Y. led the TanSat in-flight operation.

References

Bösch, H., Toon, G. C., Sen, B., Washenfelder, R. A., Wennberg, P. O., Buchwitz, M., de Beek, R., Burrows, J. P., Crisp, D., Christi, M., Connor, B. J., Natraj, V., and Yung, Y. L.: Space-based near-infrared CO2 measurements: Testing the Orbiting Carbon Observatory retrieval algorithm and validation concept using SCIAMACHY observations over Park Falls, Wisconsin, J. Geophys. Res. Atmos., 111, 1–17, https://doi.org/10.1029/2006JD007080, 2006.

Cai, Z. N., Liu, Y., and Yang, D. X.: Analysis of XCO2 retrieval sensitivity using simulated Chinese Carbon Satellite (TanSat) measurements, Sci. China Earth Sci., 57, 1919–1928, https://doi.org/10.1007/s11430-013-4707-1, 2014.

Chen, A., Mao, J., Ricciuto, D., Xiao, J., Frankenberg, C., Li, X., Thornton, P. E., Gu, L., and Knapp, A. K.: Moisture availability mediates the relationship between terrestrial gross primary production and solar-induced chlorophyll fluorescence: Insights from global-scale variations, Glob. Chang. Biol., 1–13, https://doi.org/10.1111/gcb.15373, 2020.

Dee, D. P., Uppala, S. M., Simmons, A. J., Berrisford, P., Poli, P., Kobayashi, S.: The ERA‐interim reanalysis: Configuration and performance of the data assimilation system. Q. J. R. Meteorol. Soc., 137(656), 553–597, https://doi.org/ 10.1002/qj.828, 2011.

Doughty, R., Köhler, P., Frankenberg, C., Magney, T. S., Xiao, X., Qin, Y., Wu, X., and Moore, B.: TROPOMI reveals dry-season increase of solar-induced chlorophyll fluorescence in the Amazon forest, Proc. Natl. Acad. Sci. U. S. A., 116, 22393–22398, https://doi.org/10.1073/pnas.1908157116, 2019.

398   Drusch, M., Moreno, J., del Bello, U., Franco, R., Goulas, Y., Huth, A., Kraft, S., Middleton, E. M., Miglietta, F., Mohammed,

399   G.: The FLuorescence EXplorer Mission Concept—ESA's Earth Explorer 8, ITGRS, 55, 1273–1284,

400   http://doi.org./10.1109/TGRS.2016.2621820, 2017.

401   Du, S., Liu, L., Liu, X., Zhang, X., Zhang, X., Bi, Y., and Zhang, L.: Retrieval of global terrestrial solar-induced chlorophyll

402   fluorescence from TanSat satellite, Sci. Bull., 63, 1502–1512, https://doi.org/10.1016/j.scib.2018.10.003, 2018.

403   Frankenberg, C., Butz, A., and Toon, G. C.: Disentangling chlorophyll fluorescence from atmospheric scattering effects in O2

404   A-band spectra of reflected sunlight, Geophys. Res. Lett., 38, 1–5, https://doi.org/10.1029/2010GL045896, 2011a.

405   Frankenberg, C., Fisher, J. B., Worden, J., Badgley, G., Saatchi, S. S., Lee, J. E., Toon, G. C., Butz, A., Jung, M., Kuze, A.,

406   and Yokota, T.: New global observations of the terrestrial carbon cycle from GOSAT: Patterns of plant fluorescence with gross

407   primary productivity, Geophys. Res. Lett., 38, 1–6, https://doi.org/10.1029/2011GL048738, 2011b.

408   Frankenberg, C., O'Dell, C., Berry, J., Guanter, L., Joiner, J., Köhler, P., Pollock, R., and Taylor, T. E.: Prospects for

409   chlorophyll fluorescence remote sensing from the Orbiting Carbon Observatory-2, Remote Sens. Environ., 147, 1–12,

410   https://doi.org/10.1016/j.rse.2014.02.007, 2014a.

411   Frankenberg, C., O'Dell, C., Guanter, L., and McDuffie, J.: Remote sensing of near-infrared chlorophyll fluorescence from

412   space in scattering atmospheres: Implications for its retrieval and interferences with atmospheric CO 2 retrievals, Atmos. Meas.

413   Tech., 5, 2081–2094, https://doi.org/10.5194/amt-5-2081-2012, 2012.

414   Frankenberg, C.: OCO-2 Algorithm Theoretical Basis Document: IMAP-DOAS pre-processor, 2014b.

415   Guanter, L., Aben, I., Tol, P., Krijger, J. M., Hollstein, A., Köhler, P., Damm, A., Joiner, J., Frankenberg, C., and Landgraf,

416   J.: Potential of the TROPOspheric Monitoring Instrument (TROPOMI) onboard the Sentinel-5 Precursor for the monitoring

417   of terrestrial chlorophyll fluorescence, https://doi.org/10.5194/amt-8-1337-2015, 2015.

418   Guanter, L., Alonso, L., Gómez-Chova, L., Amorós-López, J., Vila, J., and Moreno, J.: Estimation of solar-induced vegetation

419   fluorescence from space measurements, Geophys. Res. Lett., 34, 1–5, https://doi.org/10.1029/2007GL029289, 2007.

420   Guanter, L., Frankenberg, C., Dudhia, A., Lewis, P. E., Gómez-Dans, J., Kuze, A., Suto, H., and Grainger, R. G.: Retrieval

421   and global assessment of terrestrial chlorophyll fluorescence from GOSAT space measurements, Remote Sens. Environ., 121,

422   236–251, https://doi.org/10.1016/j.rse.2012.02.006, 2012.

423   Guanter, L., Zhang, Y., Jung, M., Joiner, J., Voigt, M., Berry, J. A., Frankenberg, C., Huete, A. R., Zarco-Tejada, P., Lee, J.

424   E., Moran, M. S., Ponce-Campos, G., Beer, C., Camps-Valls, G., Buchmann, N., Gianelle, D., Klumpp, K., Cescatti, A., Baker,

425   J. M., and Griffis, T. J.: Global and time-resolved monitoring of crop photosynthesis with chlorophyll fluorescence, Proc. Natl.

426   Acad. Sci. U. S. A., 111, https://doi.org/10.1073/pnas.1320008111, 2014.

427   Joiner, J., Guanter, L., Lindstrot, R., Voigt, M., Vasilkov, A. P., Middleton, E. M., Huemmrich, K. F., Yoshida, Y., and

428   Frankenberg, C.: Global monitoring of terrestrial chlorophyll fluorescence from moderate-spectral-resolution near-infrared

429   satellite measurements: methodology, simulations, and application to GOME-2, Atmos. Meas. Tech., 6, 2803–2823,

430   https://doi.org/10.5194/amt-6-2803-2013, 2013.

Joiner, J., Yoshida, Y., Guanter, L., and Middleton, E. M.: New methods for the retrieval of chlorophyll red fluorescence from hyperspectral satellite instruments: simulations and application to GOME-2 and SCIAMACHY, Atmos. Meas. Tech., 9, 3939–3967, https://doi.org/10.5194/amt-9-3939-2016, 2016.

Joiner, J., Yoshida, Y., Vasilkov, A. P., Middleton, E. M., Campbell, P. K. E., Yoshida, Y., Kuze, A., and Corp, L. A.: Filling-in of near-infrared solar lines by terrestrial fluorescence and other geophysical effects: simulations and space-based observations from SCIAMACHY and GOSAT, Atmos. Meas. Tech., 5, 809–829, https://doi.org/10.5194/amt-5-809-2012, 2012.

Joiner, J., Yoshida, Y., Vasilkov, A. P., Yoshida, Y., Corp, L. A., and Middleton, E. M.: First observations of global and seasonal terrestrial chlorophyll fluorescence from space, 8, 637–651, https://doi.org/10.5194/bg-8-637-2011, 2011.

Joiner, J., Yoshida, Y., Zhang, Y., Duveiller, G., Jung, M., Lyapustin, A., Wang, Y., and Tucker, C. J.: Estimation of terrestrial global gross primary production (GPP) with satellite data-driven models and eddy covariance flux data, Remote Sens., 10, 1–38, https://doi.org/10.3390/rs10091346, 2018.

Jung, M., Schwalm, C., Migliavacca, M., Walther, S., Camps-Valls, G., Koirala, S., Anthoni, P., Besnard, S., Bodesheim, P., Carvalhais, N., Chevallier, F., Gans, F., S Goll, D., Haverd, V., Köhler, P., Ichii, K., K Jain, A., Liu, J., Lombardozzi, D., E M S Nabel, J., A Nelson, J., O'Sullivan, M., Pallandt, M., Papale, D., Peters, W., Pongratz, J., Rödenbeck, C., Sitch, S., Tramontana, G., Walker, A., Weber, U., and Reichstein, M.: Scaling carbon fluxes from eddy covariance sites to globe: Synthesis and evaluation of the FLUXCOM approach, 17, 1343–1365, https://doi.org/10.5194/bg-17-1343-2020, 2020.

Köhler, P., Frankenberg, C., Magney, T. S., Guanter, L., Joiner, J., and Landgraf, J.: Global Retrievals of Solar-Induced Chlorophyll Fluorescence With TROPOMI: First Results and Intersensor Comparison to OCO-2, Geophys. Res. Lett., 45, 10,456-10,463, https://doi.org/10.1029/2018GL079031, 2018b.

Köhler, P., Guanter, L., and Joiner, J.: A linear method for the retrieval of sun-induced chlorophyll fluorescence from GOME-2 and SCIAMACHY data, Atmos. Meas. Tech., 8, 2589–2608, https://doi.org/10.5194/amt-8-2589-2015, 2015.

Köhler, P., Guanter, L., Kobayashi, H., Walther, S., and Yang, W.: Assessing the potential of sun-induced fluorescence and the canopy scattering coefficient to track large-scale vegetation dynamics in Amazon forests, Remote Sens. Environ., 204, 769–785, https://doi.org/10.1016/j.rse.2017.09.025, 2018a.

Lee, J. E., Frankenberg, C., Van Der Tol, C., Berry, J. A., Guanter, L., Boyce, C. K., Fisher, J. B., Morrow, E., Worden, J. R., Asefi, S., Badgley, G., and Saatchi, S.: Forest productivity and water stress in Amazonia: Observations from GOSAT chlorophyll fluorescence, Tohoku J. Exp. Med., 230, https://doi.org/10.1098/rspb.2013.0171, 2013.

Li, X., Xiao, J., and He, B.: Chlorophyll fluorescence observed by OCO-2 is strongly related to gross primary productivity estimated from flux towers in temperate forests, Remote Sens. Environ., 204, 659–671, https://doi.org/10.1016/j.rse.2017.09.034, 2018.

Li, X., Xiao, J., Kimball, J. S., Reichle, R. H., Scott, R. L., Litvak, M. E., Bohrer, G., and Frankenberg, C.: Synergistic use of SMAP and OCO-2 data in assessing the responses of ecosystem productivity to the 2018 U.S. drought, Remote Sens. Environ., 251, 112062, https://doi.org/10.1016/j.rse.2020.112062, 2020.

465 Liu, X., Guanter, L., Liu, L., Damm, A., Malenovský, Z., Rascher, U., Peng, D., Du, S., and Gastellu-Etchegorry, J. P.:
466 Downscaling of solar-induced chlorophyll fluorescence from canopy level to photosystem level using a random forest model,
467 Remote Sens. Environ., 231, 110772, https://doi.org/10.1016/j.rse.2018.05.035, 2019.

468 Liu, Y., Wang, J., Yao, L., Chen, X., Cai, Z., Yang, D., Yin, Z., Gu, S., Tian, L., Lu, N., and Lyu, D.: The TanSat mission:
469 preliminary global observations, Sci. Bull., 63, 1200–1207, https://doi.org/10.1016/j.scib.2018.08.004, 2018.

470 MacBean, N., Maignan, F., Bacour, C., Lewis, P., Peylin, P., Guanter, L., Köhler, P., Gómez-Dans, J., and Disney, M.: Strong
471 constraint on modelled global carbon uptake using solar-induced chlorophyll fluorescence data, Sci. Rep., 8, 1–12,
472 https://doi.org/10.1038/s41598-018-20024-w, 2018.

473 NASA JPL. NASA Shuttle Radar Topography Mission Global 30 arc second [Data set]. NASA EOSDIS Land Processes
474 DAAC. Accessed 2022-02-27 from https://doi.org/10.5067/MEaSUREs/SRTM/SRTMGL30.002, 2013.

475 O'Dell, C. W., Connor, B., Bösch, H., O'Brien, D., Frankenberg, C., Castano, R., Christi, M., Eldering, D., Fisher, B., Gunson,
476 M., McDuffie, J., Miller, C. E., Natraj, V., Oyafuso, F., Polonsky, I., Smyth, M., Taylor, T., Toon, G. C., Wennberg, P. O.,
477 and Wunch, D.: The ACOS CO2 retrieval algorithm-Part 1: Description and validation against synthetic observations, Atmos.
478 Meas. Tech., 5, 99–121, https://doi.org/10.5194/amt-5-99-2012, 2012.

479 Qiu, R., Han, G., Ma, X., Xu, H., Shi, T., and Zhang, M.: A comparison of OCO-2 SIF, MODIS GPP, and GOSIF data from
480 gross primary production (GPP) estimation and seasonal cycles in North America, Remote Sens., 12,
481 https://doi.org/10.3390/rs12020258, 2020.

482 Reuter, M., Buchwitz, M., Schneising, O., Heymann, J., Bovensmann, H., and Burrows, J. P.: A method for improved
483 SCIAMACHY CO_2 retrieval in the presence of optically thin clouds, Atmos. Meas. Tech., 3, 209–232,
484 https://doi.org/10.5194/amt-3-209-2010, 2010.

485 Sun, K., Liu, X., Nowlan, C. R., Cai, Z., Chance, K., Frankenberg, C., Lee, R. A. M., Pollock, R., Rosenberg, R., and Crisp,
486 D.: Characterization of the OCO-2 instrument line shape functions using on-orbit solar measurements, Atmos. Meas. Tech.,
487 10, 939–953, https://doi.org/10.5194/amt-10-939-2017, 2017b.

488 Sun, Y., Frankenberg, C., Jung, M., Joiner, J., Guanter, L., Köhler, P., and Magney, T.: Overview of Solar-Induced chlorophyll
489 Fluorescence (SIF) from the Orbiting Carbon Observatory-2: Retrieval, cross-mission comparison, and global monitoring for
490 GPP, Remote Sens. Environ., 209, 808–823, https://doi.org/10.1016/j.rse.2018.02.016, 2018.

491 Sun, Y., Frankenberg, C., Wood, J. D., Schimel, D. S., Jung, M., Guanter, L., Drewry, D. T., Verma, M., Porcar-Castell, A.,
492 Griffis, T. J., Gu, L., Magney, T. S., Köhler, P., Evans, B., and Yuen, K.: OCO-2 advances photosynthesis observation from
493 space via solar-induced chlorophyll fluorescence, Science (80-.)., 358, https://doi.org/10.1126/science.aam5747, 2017a.

494 Sun, Y., Fu, R., Dickinson, R., Joiner, J., Frankenberg, C., Gu, L., Xia, Y., and Fernando, N.: Drought onset mechanisms
495 revealed by satellite solar-induced chlorophyll fluorescence: Insights from two contrasting extreme events, J. Geophys. Res.
496 G Biogeosciences, 120, 2427–2440, https://doi.org/10.1002/2015JG003150, 2015.

497   Tramontana, G., Jung, M., Schwalm, C. R., Ichii, K., Camps-Valls, G., Ráduly, B., Reichstein, M., Arain, M. A., Cescatti, A.,

498   Kiely, G., Merbold, L., Serrano-Ortiz, P., Sickert, S., Wolf, S., and Papale, D.: Predicting carbon dioxide and energy fluxes

499   across global FLUXNET sites with regression algorithms, 13, 4291–4313, https://doi.org/10.5194/bg-13-4291-2016, 2016.

500   van der Tol, C., Rossini, M., Cogliati, S., Verhoef, W., Colombo, R., Rascher, U., and Mohammed, G.: A model and

501   measurement comparison of diurnal cycles of sun-induced chlorophyll fluorescence of crops, Remote Sens. Environ., 186,

502   663–677, https://doi.org/10.1016/j.rse.2016.09.021, 2016.

503   Yang, D., Boesch, H., Liu, Y., Somkuti, P., Cai, Z., Chen, X., Di Noia, A., Lin, C., Lu, N., Lyu, D., Parker, R. J., Tian, L.,

504   Wang, M., Webb, A., Yao, L., Yin, Z., Zheng, Y., Deutscher, N. M., Griffith, D. W. T., Hase, F., Kivi, R., Morino, I., Notholt,

505   J., Ohyama, H., Pollard, D. F., Shiomi, K., Sussmann, R., Té, Y., Velazco, V. A., Warneke, T., and Wunch, D.: Toward High

506   Precision XCO2 Retrievals From TanSat Observations: Retrieval Improvement and Validation Against TCCON

507   Measurements, J. Geophys. Res. Atmos., 125, 1–26, https://doi.org/10.1029/2020JD032794, 2020.

508   Yang, D., Liu, Y., Boesch, H., Yao, L., Di Noia, A., Cai, Z., Lu, N., Lyu, D., Wang, M., Wang, J., Yin, Z., and Zheng, Y.: A

509   New TanSat XCO2 Global Product towards Climate Studies, Adv. Atmos. Sci., 38, 8–11, https://doi.org/10.1007/s00376-020-

510   0297-y, 2021.

511   Yang, D., Liu, Y., Cai, Z., Chen, X., Yao, L., and Lu, D.: First Global Carbon Dioxide Maps Produced from TanSat

512   Measurements, Adv. Atmos. Sci., 35, 621–623, https://doi.org/10.1007/s00376-018-7312-6, 2018.

513   Yang, D., Liu, Y., Cai, Z., Deng, J., Wang, J., and Chen, X.: An advanced carbon dioxide retrieval algorithm for satellite

514   measurements and its application to GOSAT observations, Sci. Bull., 60, 2063–2066, https://doi.org/10.1007/s11434-015-

515   0953-2, 2015b.

516   Yang, X., Tang, J., Mustard, J. F., Lee, J. E., Rossini, M., Joiner, J., Munger, J. W., Kornfeld, A., and Richardson, A. D.: Solar-

517   induced chlorophyll fluorescence that correlates with canopy photosynthesis on diurnal and seasonal scales in a temperate

518   deciduous forest, Geophys. Res. Lett., 42, 2977–2987, https://doi.org/10.1002/2015GL063201, 2015a.

519   Yao, L., Yang, D., Liu, Y., Wang, J., Liu, L., Du, S., Cai, Z., Lu, N., Lyu, D., Wang, M., Yin, Z., and Zheng, Y.: A New

520   Global Solar-induced Chlorophyll Fluorescence (SIF) Data Product from TanSat Measurements, Adv. Atmos. Sci., 38, 341–

521   345, https://doi.org/10.1007/s00376-020-0204-6, 2021.

522   Yin, Y., Byrne, B., Liu, J., Wennberg, P. O., Davis, K. J., Magney, T., Köhler, P., He, L., Jeyaram, R., Humphrey, V., Gerken,

523   T., Feng, S., Digangi, J. P., and Frankenberg, C.: Cropland Carbon Uptake Delayed and Reduced by 2019 Midwest Floods,

524   AGU Adv., 1, 1–15, https://doi.org/10.1029/2019av000140, 2020.

525   Yoshida, Y., Joiner, J., Tucker, C., Berry, J., Lee, J. E., Walker, G., Reichle, R., Koster, R., Lyapustin, A., and Wang, Y.: The

526   2010 Russian drought impact on satellite measurements of solar-induced chlorophyll fluorescence: Insights from modeling

527   and comparisons with parameters derived from satellite reflectances, Remote Sens. Environ., 166, 163–177,

528   https://doi.org/10.1016/j.rse.2015.06.008, 2015.

529   Yoshida, Y., Kikuchi, N., Morino, I., Uchino, O., Oshchepkov, S., Bril, A., Saeki, T., Schutgens, N., Toon, G. C., Wunch, D.,

530   Roehl, C. M., Wennberg, P. O., Griffith, D. W. T., Deutscher, N. M., Warneke, T., Notholt, J., Robinson, J., Sherlock, V.,

531 Connor, B., Rettinger, M., Sussmann, R., Ahonen, P., Heikkinen, P., Kyrö, E., Mendonca, J., Strong, K., Hase, F., Dohe, S.,

532 and Yokota, T.: Improvement of the retrieval algorithm for GOSAT SWIR XCO2and XCH4and their validation using TCCON

533 data, Atmos. Meas. Tech., 6, 1533–1547, https://doi.org/10.5194/amt-6-1533-2013, 2013.

534 Yoshida, Y., Ota, Y., Eguchi, N., Kikuchi, N., Nobuta, K., Tran, H., Morino, I., and Yokota, T.: Retrieval algorithm for CO_2

535 and CH_4 column abundances from short-wavelength infrared spectral observations by the Greenhouse gases observing satellite,

536 Atmos. Meas. Tech., 4, 717–734, https://doi.org/10.5194/amt-4-717-2011, 2011.

537 Yu, L., Wen, J., Chang, C. Y., Frankenberg, C., and Sun, Y.: High-Resolution Global Contiguous SIF of OCO-2, Geophys.

538 Res. Lett., 46, 1449–1458, https://doi.org/10.1029/2018GL081109, 2019.

539 Zhang, Y., Guanter, L., Berry, J. A., Joiner, J., van der Tol, C., Huete, A., Gitelson, A., Voigt, M., and Köhler, P.: Estimation

540 of vegetation photosynthetic capacity from space-based measurements of chlorophyll fluorescence for terrestrial biosphere

541 models, Glob. Chang. Biol., 20, 3727–3742, https://doi.org/10.1111/gcb.12664, 2014.

542 Zhang, Y., Xiao, X., Zhang, Y., Wolf, S., Zhou, S., Joiner, J., Guanter, L., Verma, M., Sun, Y., Yang, X., Paul-Limoges, E.,

543 Gough, C. M., Wohlfahrt, G., Gioli, B., van der Tol, C., Yann, N., Lund, M., and de Grandcourt, A.: On the relationship

544 between sub-daily instantaneous and daily total gross primary production: Implications for interpreting satellite-based SIF

545 retrievals, Remote Sens. Environ., 205, 276–289, https://doi.org/10.1016/j.rse.2017.12.009, 2018.